Extremely Large Magnetoresistance in a Topological Semimetal Candidate Pyrite $PtBi_2$

Wenshuai Gao,[1,2] Ningning Hao,[1] Fa-Wei Zheng,[3] Wei Ning,[1,*] Min Wu,[1,2] Xiangde Zhu,[1,†] Guolin Zheng,[1,2] Jinglei Zhang,[1] Jianwei Lu,[1,2] Hongwei Zhang,[1,2] Chuanying Xi,[1] Jiyong Yang,[1] Haifeng Du,[1] Ping Zhang,[3,4] Yuheng Zhang,[1,5] and Mingliang Tian[1,5,‡]

[1]*Anhui Province Key Laboratory of Condensed Matter Physics at Extreme Conditions, High Magnetic Field Laboratory, Chinese Academy of Sciences, Hefei 230031, Anhui, People's Republic of China.*

[2]*Department of Physics, University of Science and Technology of China, Hefei 230026, People's Republic of China*

[3]*Institute of Applied Physics and Computational Mathematics, Beijing 100088, People's Republic of China*

[4]*Beijing Computational Science Research Center, Beijing 100193, People's Republic of China*

[5]*Collaborative Innovation Center of Advanced Microstructures, Nanjing University, Nanjing 210093, People's Republic of China*

(Received 6 September 2016; revised manuscript received 14 March 2017; published 23 June 2017)

While pyrite-type $PtBi_2$ with a face-centered cubic structure has been predicted to be a three-dimensional (3D) Dirac semimetal, experimental study of its physical properties remains absent. Here we report the angular-dependent magnetoresistance measurements of a $PtBi_2$ single crystal under high magnetic fields. We observed extremely large unsaturated magnetoresistance (XMR) up to $(11.2\times10^6)\%$ at $T = 1.8$ K in a magnetic field of 33 T, which is comparable to the previously reported Dirac materials, such as WTe_2, LaSb, and NbP. The crystals exhibit an ultrahigh mobility and significant Shubnikov–de Hass quantum oscillations with a nontrivial Berry phase. The analysis of Hall resistivity indicates that the XMR can be ascribed to the nearly compensated electron and hole. Our experimental results associated with the *ab initio* calculations suggest that pyrite $PtBi_2$ is a topological semimetal candidate that might provide a platform for exploring topological materials with XMR in noble metal alloys.

DOI: 10.1103/PhysRevLett.118.256601

Recently discovered three-dimensional (3D) Dirac and Weyl semimetals represent a new state of topological quantum matter. These materials are characterized with a linear energy dispersion in bulk and can be viewed as "3D graphene" [1–5]. The Dirac point can be viewed as a pair of Weyl points coinciding in momentum space, protected by time-reversal, space inversion, as well as crystalline point-group symmetries [3–6]. Dirac semimetals can be evolved into Weyl semimetals when either time-reversal symmetry or space inversion symmetry is broken. Several materials have been confirmed to be Dirac semimetals, such as Cd_3As_2 [7–11] and Na_3Bi [12,13]. In addition, WTe_2 [14], TaAs [15–17], NbAs [18], TaP [19], and NbP [20] have also been experimentally suggested to be Weyl semimetals. The unique band structures of these materials result in peculiar quantum phenomena, such as ultrahigh carrier mobility [21–23] and very large nonsaturating magnetoresistance (MR) [21,22]. These appealing transport properties have generated immense interest in both condensed matter physics and its potential application.

Discovering new Dirac materials with novel properties has become an important front in condensed matter and material sciences. Pyrite-type $PtBi_2$ has been theoretically predicted to be a new 3D Dirac semimetal by Gibson *et al.* [24], and it has a face-centered cubic structure with a broken inversion symmetry. The different C_3 rotation eigenvalues result in band crossing and, consequently, a 3D Dirac point along the line Γ-R; thus, interesting physics or phenomena are expected in the noble alloy. Motivated by this prediction, we grew high-quality pyrite-type $PtBi_2$ single crystals and carried out a detailed magnetotransport study. Under magnetic field up to 33 T, we observed extremely large MR (XMR) up to $(11.2\times10^6)\%$ at 1.8 K without any sign of saturation, which is higher than WTe_2 and any other similar Dirac materials reported before [14,25,26]. Significant Shubnikov–de Hass (SdH) quantum oscillations develop at low temperatures which enables us to reconstruct the Fermi surface topology in $PtBi_2$. The analysis of Hall resistivity indicates that the XMR can be ascribed to the nearly compensated electron and hole with high mobility at low temperatures. Our experimental results associated with the *ab initio* calculation suggest that pyrite $PtBi_2$ is a topological semimetal candidate with unique band structure.

The cubic system $PtBi_2$ crystallizes in a pyrite-type structure with a space group of $Pa\bar{3}$. The a, b, c axes are perpendicular to each other, and the lattice parameters are $a = b = c = 6.702$ Å as shown in Fig. 1(a). The samples were prepared by the flux method, and the detailed growing processes will be published elsewhere. The inset of Fig. 1(b) is the morphology of a crystal with a (111) facet. Figure 1(b) shows x-ray diffraction oriented with the scattering vector perpendicular to the (111) plane. Magnetotransport measurements were carried out in the (111) plane using both a 16 T physical property measurement system (Quantum Design Inc.) and the ~35 T dc-resistive magnet at the China High Magnetic Field Laboratory in Hefei.

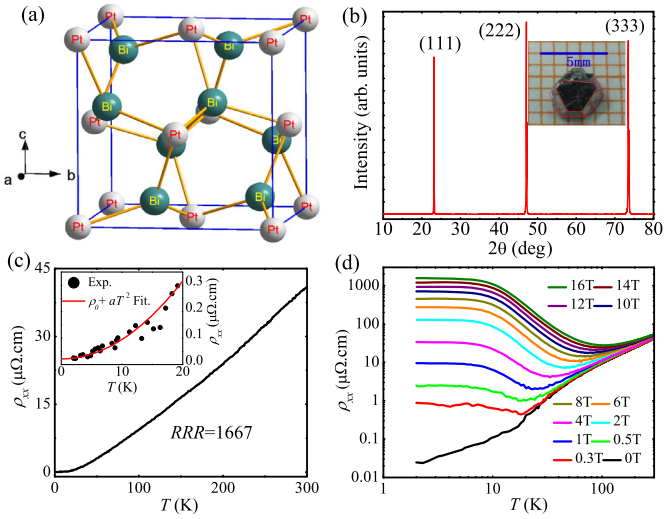

FIG. 1. (a) The crystal structure of pyrite-type $PtBi_2$ with cubic symmetry and space group of $Pa\bar{3}$. Gray and cyan balls represent the Pt atom and Bi atom, respectively. (b) The x-ray diffraction pattern of a pyrite-type $PtBi_2$ single crystal. Inset: Photo of a typical $PtBi_2$ single crystal. (a) Temperature dependence of the longitudinal resistivity ρ_{xx} from 2 to 300 K at zero magnetic field. Inset: The zero-field resistivity curve below 20 K can be well fitted by the formula $\rho = \rho_0 + aT^2$. (b) Temperature dependence of resistivity at various magnetic fields applied perpendicular to the (111) plane and current.

Figure 1(c) describes the temperature dependence of the longitudinal resistivity ρ_{xx} of a sample from 2 to 300 K at zero magnetic field. The resistivity exhibits highly metallic behavior with $\rho_{xx}(300\ \mathrm{K}) = 40\ \mu\Omega\cdot\mathrm{cm}$ and $\rho_{xx}(2\ \mathrm{K}) = 24\ \mathrm{n}\Omega\cdot\mathrm{cm}$, leading to an extremely large residual resistance ratio (RRR), $R(300\ \mathrm{K})/R\ (2\mathrm{K}) = 1667$. This result indicates that the $PtBi_2$ crystal studied here is high quality. The zero-field resistivity curve below 20 K can be well fitted by formula $\rho = \rho_0 + aT^2$, as shown in the inset of Fig. 1(c), where the residual resistivity ρ_0 is about 18 $\mathrm{n}\Omega\cdot\mathrm{cm}$. When a small magnetic field of 0.3 T is applied perpendicular to the (111) plane, the R-T curve displays a metal-insulator transition (MIT) driven by magnetic field [Fig. 1(d)] and develops a resistivity plateau at low temperature. The insulating behavior is enhanced significantly as the magnetic field increases. Such a "turn-on" and plateau behaviors at low temperatures in $PtBi_2$ are very similar to those reported in other semimetals, such as WTe_2 [14,28], NbP [21], and LaSb [26]. Detailed analysis of the R-T curves under magnetic fields can be found in the Supplement Material [27].

Figure 2(a) shows the MR under different temperatures with the field perpendicular to the high symmetry (111) plane. An extremely large MR, $[(R(B) - R(0))/R(0)] \times 100\% \sim (1.12 \times 10^7)\%$ is observed under 33 T at 1.8 K, which is accompanied with clear SdH quantum oscillations. This huge MR value is comparable to those in topological semimetals WTe_2, LaSb, and NbP, where the MR is, respectively, about $(1.3 \times 10^7)\%$ under 60 T at 0.53 K [14], $\sim(1 \times 10^6)\%$ at 9 T [26], and $\sim(8.1 \times 10^6)\%$ under 62 T at 1.5 K [21]. Such a large MR puts $PtBi_2$ successively in the category of the largest MR materials. Considering that the MR of $PtSn_4$ [29], the only noble metal alloy showing XMR previously, is just about $(5 \times 10^5)\%$ at 1.8 K and 14 T, $PtBi_2$ is definitely the first noble metal alloy with a MR on the scale of more than 10^6. Furthermore, the MR in $PtBi_2$ does not reach a saturation up to 33 T. In addition to the large magnitude, following a conventional quadratic dependence in low fields, a linear MR is also observed in our $PtBi_2$ single crystals from $B = 14$ T up to 33 T. For such a linear field dependence, the MR could reach $(2.2 \times 10^7)\%$ if the field is further increased to 60 T, which is even higher than WTe_2. Such a linear field dependence for MR is also widely observed in these Dirac-Weyl semimetals. We have measured another sample with lower quality which shows $RRR = 524$ and residual resistance $\rho_0 = 77\ \mathrm{n}\Omega\cdot\mathrm{cm}$. The XMR of this sample is 3.3×10^6 at 33 T with a saturation trend at high field range (not shown), indicating that the crystal quality is very crucial in boosting XMR.

In order to obtain more information on the electronic structure of the $PtBi_2$, we have investigated the quantum oscillations at different temperatures with the field perpendicular to the high symmetry (111) plane. Figure 2(b) shows the SdH oscillation spectra of ρ_{xx} in the (111) plane after subtracting a third-order polynomial background. The oscillation amplitudes decrease gradually with increasing temperature. As shown in the inset of Fig. 2(b), the fast Fourier transform (FFT) spectra of SdH oscillations reveal two principal frequencies $F_\alpha = 250$ T and $F_\beta = 850$ T. The F_β peak emerges at about 10 K and increases rapidly upon cooling. According to the Onsager relation $F = (\hbar/2\pi e)A_F$, the cross section area of Fermi surface A_F is determined to be 0.024 and 0.081 $\mathrm{Å}^{-2}$ for the α band and β band, respectively, indicating a complicated Fermi surface. Additionally, we observed peak splitting behavior in the high field oscillations above $B = 16$ T at $T = 1.8$ K, which can be clearly seen from the inset of Fig. 2(b) that shows a peak splitting between 0.032 and 0.036 T^{-1}. With increasing temperature above 15 K, the splitting gradually merges to a single peak, implying an origin of the Zeeman effect.

We have further estimated the effective masses of electrons as shown in Fig. 2(c), by fitting the temperature dependence of the oscillation amplitudes using the Lifshitz-Kosevich formula:

$$\frac{\Delta\rho(T,B)}{\rho(B=0)} \propto \frac{2\pi^2 k_B T/\hbar\omega_c}{\sinh[2\pi^2 k_B T/\hbar\omega_c]} \exp(-2\pi^2 k_B T_D/\hbar\omega_c), \quad (1)$$

where k_B is the Boltzmann constant, $\hbar$ is Planck's constant, and $\omega_c = eB/m^*$ is the cyclotron frequency, with m^* the effective cyclotron mass at the Fermi energy. We get the effective cyclotron mass $m^*_\alpha = 0.64 \pm 0.012 m_0$ and $m^*_\beta = 0.68 \pm 0.014 m_0$, respectively, with m_0 the bare electron

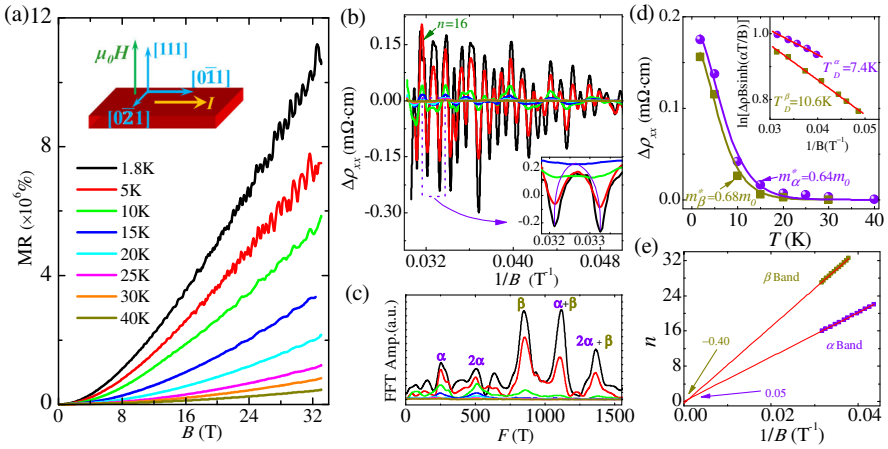

FIG. 2. (a) MR of $PtBi_2$ under different temperatures with the field applied perpendicular to the high symmetry (111) plane and current. (b) The SdH oscillation $\Delta\rho_{xx}$ plotted as a function of inverse field at different temperatures. The inset shows the Zeeman splitting of an oscillation peak at high field. Data at different temperatures have been shifted for clarity. (c) FFT spectra of SdH oscillations at different temperatures. (d) The amplitudes of the oscillatory component at various temperatures. The solid lines are fitting results of the Lifshitz-Kosevich formula. Inset: Dingle plot of the SdH oscillation associated with the α and β bands. (e) The Landau level indices extracted from the SdH oscillation plotted as a function of inverse field.

mass. Correspondingly, the Fermi velocity $v_F = \hbar k_F/m^*$ is $\sim 1.58 \times 10^5$ m/s for the α band and $\sim 2.76 \times 10^5$ m/s for the β band; thus, the Fermi energy $E_F = m^* v_F^2$ is $E_F^\alpha \sim 90.7$ meV and $E_F^\beta \sim 292.4$ meV. We have also analyzed the quantum mobility, as shown in the inset in Fig. 2(c). In Eq. (1), the T_D is the Dingle temperature which is related to the quantum scattering lifetime τ_Q by $T_D = \hbar/2\pi k_B \tau_Q$. The field dependence of the amplitude of quantum oscillations at fixed temperatures gives access to the Dingle temperature $T_D^\alpha = 7.4$ K and $T_D^\beta = 10.6$ K. The corresponding quantum scattering lifetimes are $\tau_Q^\alpha = 1.6(5) \times 10^{-13}$ s and $\tau_Q^\beta = 1.1(5) \times 10^{-13}$ s. The mobilities estimated by $\mu_Q = (e\tau_Q/m^*)$ are $\mu_Q^\alpha = 453.4$ cm^2 V^{-1} s^{-1} and $\mu_Q^\beta = 298.7$ cm^2 V^{-1} s^{-1}, respectively.

The nontrivial Berry phase is generally considered to be the key evidence for Dirac fermions and has been observed in other Dirac materials [30,31]. According to the Lifshitz-Onsager quantization rule [32], the oscillations can be described by $\Delta\rho_{xx} \propto \cos[2\pi(F/B + \phi)]$, where F is the oscillations' frequency, and ϕ is the phase shift. To extract the phase shift, a plot of the Landau index n vs $1/B$ then extrapolates to the phase shift on the n axis. The Dirac system with linear dispersion carries an extra π Berry phase, leading to phase shifts with $\phi = 0$ in the 2D system and $\pm 1/8$ in the 3D case. While for Dirac semimetals with time-reversal symmetry (e.g., $PtBi_2$), an anomalous phase shift leads the value of the phase shift ϕ changing from $\pm 1/8$ to $\pm 5/8$ [33]. Considering $PtBi_2$ is a multiband system and $\rho_{xx} \gg \rho_{xy}$, here the peak of the SdH oscillations should be defined as integer indices and the valley as half indices [34]. As shown in Fig. 3(e), the linear fitting of n vs $1/B$ gives the intercept value 0.05 ± 0.01 for the α band, which is very close to zero and suggests a topological trivial Berry phase of the α band, and -0.40 ± 0.02 for the β band [Fig. 2(e)], which is close to $-5/8$ and indicates a nontrivial Berry phase of the β band.

Figure 3(a) shows the angular-dependent MR with tilting the magnetic field from the [111] direction ($\theta = 0°$) to the $[0\bar{1}1]$ direction ($\theta = 90°$) parallel to the applied current in the (111) plane. The MR decreases dramatically from $(1.12 \times 10^7)\%$ to $(2 \times 10^4)\%$ at $B = 33$ T, indicating a significant anisotropic MR with an amplitude ratio up to $(5.6 \times 10^4)\%$. The full-range angular-dependent MR at 16 T is shown in the inset of Fig. 3(a), where a twofold rotation symmetric pattern can be clearly seen. Figure 3(b) shows the SdH oscillation spectra at different angles after subtracting the smooth background. The SdH oscillations can be observed in all angles, indicating an anisotropic 3D character of the Fermi surface (FS) in $PtBi_2$. Figure 3(c) shows the angular dependences of F_α and F_β. The frequencies of the band involve a nonmonotonic behavior as the field tilted from the [111] direction to the applied current direction in the (111) plane, indicating the complex contour of the FS of this band. Here, we just consider the α band by fitting the F_α with both the 2D FS model and the 3D standard ellipsoid FS

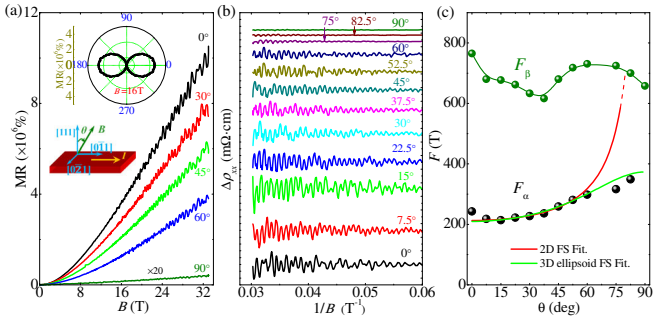

FIG. 3. (a) Magnetoresistence under different angles at $T = 2$ K. Inset shows the polar plot for the MR under 16 T and 2 K. (b) SdH patterns at various angles plotted as a function of inverse field. (c) The angular dependence of the oscillation frequency derived from FFT analysis from (b). The solid lines are the fits to the Fermi surfaces using the 2D Fermi surface and 3D ellipsoid Fermi surface models.

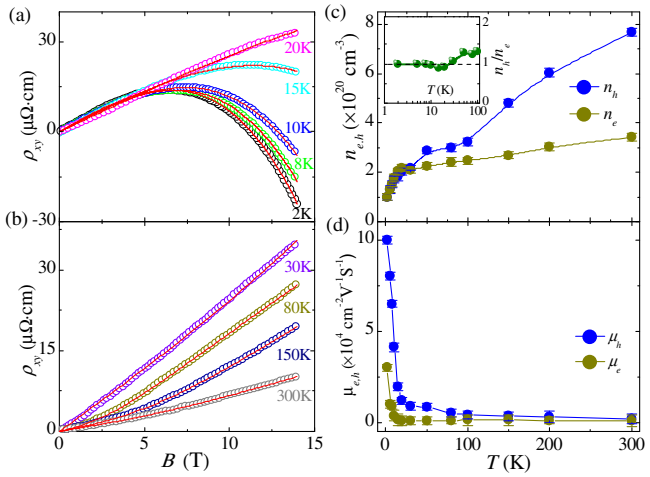

FIG. 4. (a),(b) Hall resistivity ρ_{xy} at several typical temperatures. The red solid lines are numerical fittings to the two-band model. (c) Temperature dependence of the carrier density $n_{e,h}$. Inset: The ratio of n_h/n_e at low temperatures. (d) Temperature dependence of the mobility $\mu_{e,h}$.

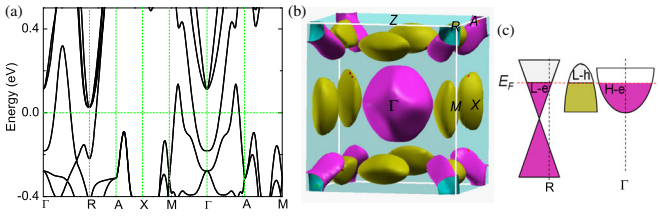

FIG. 5. (a),(b) The *ab initio* band structure and bulk Fermi surface of pyrite-type $PtBi_2$. (c) Schematic illustration of the semimetal hosted by pyrite-type $PtBi_2$. The pink and yellow colors correspond to (b) and label the electron and hole bands, respectively. "L-e," "L-h," and "H-e" label the light electron, light hole, and heavy electron with small and large effective mass, respectively.

model, and find that the 3D ellipsoid FS can reproduce the data better, consistent with the expectation of the anisotropic 3D FS.

To further investigate the transport properties of $PtBi_2$, we systemically measured the Hall resistivity at different temperatures. Several selected curves are shown in Figs. 4(a) and 4(b). Above 30 K, the Hall resistivity ρ_{xy} is positive, indicating the hole-type carriers dominate the transport behavior. When lowering the temperatures, the Hall resistivity keeps positive at low field but becomes negative in slope at higher fields, indicating a multiband effect in $PtBi_2$. For simplicity, here a typical two-band model Eq. (2) was used to describe the Hall effect in the full temperature range,

$$\rho_{xy}(B) = \frac{B}{e}\frac{(n_h\mu_h^2 - n_e\mu_e^2) + (n_h - n_e)\mu_h^2\mu_e^2B^2}{(n_h\mu_h + n_e\mu_e)^2 + (n_h - n_e)^2\mu_h^2\mu_e^2B^2}, \quad (2)$$

where the n_h, n_e, μ_h, and μ_e are the carrier concentrations and mobilities of the electron and hole, respectively. The obtained $n_{h,e}$ and $\mu_{h,e}$ as a function of the temperature are shown in Figs. 4(c) and 4(d). It can be found that both n_h and n_e decrease monotonically with decreasing temperature with a opposite trend of $\mu_{h,e}$. At 2 K, the carriers' concentration reaches $n_h \approx 0.99(8) \times 10^{20}$ cm^{-3} and $n_e \approx 1.0(1) \times 10^{20}$ cm^{-3}. Such densities are similar to WTe_2 [14] and LaSb [26] but 2 orders higher than Cd_3As_2 [11], NbP [21], and NbAs [35]. We note that the ratio of n_h/n_e in $PtBi_2$ is also close to 1 below 30 K, indicating that the carriers of the holes and electrons are nearly compensated in the low-temperature range, which is similar to WTe_2 [14] and NbAs [33]. We now turn to the classical transport mobility extracted from Hall resistivity. Above 30 K, the transport mobility for both carriers shows weak temperature dependence. However, as the temperature decreases to 2 K, the mobility increases dramatically to 1.0×10^5 cm^2 V^{-1} s^{-1} and 0.31×10^5 cm^2 V^{-1} s^{-1} for the hole and electron, respectively. This value is lower than NbP and Cd_3As_2 but comparable to WTe_2, LaSb, NbAs, and TaAs. However, our MR ratio is higher than these materials, and, thus, we inferred that the extremely large *RRR* (~1667) in our $PtBi_2$ may play an important role in boosting the highest XMR. Additionally, we note that the Hall mobility is about 2 orders higher than the quantum mobility obtained from the SdH oscillations. Such a deviation has been observed in other topological semimetals such as Cd_3As_2 [11], NbAs [33], and might be associated with the different scattering processes. It is known that the quantum mobility is sensitive to all angle scattering processes, while the classical transport mobility is only susceptible to the large angle scattering process. The ratio τ_{tr}/τ_Q is a measure of the relative importance of small angle scattering. According to the aforementioned experimental results, the transport lifetimes $\tau_{tr} = (\mu m^*/e)$ for the two pockets can be estimated to be $\tau_{tr}^{\alpha} \sim 3.64 \times 10^{-11}$ s and $\tau_{tr}^{\beta} \sim 1.1(5) \times 10^{-11}$ s. The large ratio of $\tau_{tr}/\tau_Q > 100$ suggests that the backward scattering is reduced severely, and the small angle scattering is dominated in $PtBi_2$.

To further understand the transport properties and verify the Dirac physics in $PtBi_2$, we have carefully performed an *ab initio* calculation to obtain the electronic structure. The band structure is calculated by density functional theory and fully relaxed atomic coordinates. As the result shown in Fig. 5, there are three pockets, including two electron pockets located around the Γ point and *R* point, respectively, and one hole pocket crossed by the Γ-*M* line (actually, there are 12 hole pockets in the first Brillouin zone, but they are equivalent and can be counted as one.). The coexistence of the electron and hole is consistent with the Hall resistivity results. However, only two Fermi pockets have been identified from the FFT spectra of SdH oscillations (shown in Fig. 2). The reason might lie in the fact that the electrons from this pocket have a much larger effective cyclotron mass, which is estimated to be

10 times the effective mass of the hole band, i.e., $6.4\,m_0$, from the band structure and respond insensitively to the external magnetic field and, thus, cannot be identified from the FFT spectra of SdH oscillations. From Fig. 5(a), we find that there is a Dirac point located ~230 meV below the Fermi level, which is close to our aforementioned experimental fitting result of $E_F^{\beta} \sim 292.4$ meV. Meanwhile, the band top of the hole band to the Fermi level is about 130 meV, which is also close to $E_F^{\alpha} \sim 90.7$ meV. This result also indicates that the α and β Fermi pockets correspond, respectively, to the hole pocket and electron pocket around the R point. Such correspondence also coincides with the angular dependence of the oscillation frequency in Fig. 3(c) that the β pocket is anisotropic while the α pocket can be approximately described by an ellipsoid. Finally, we plot a schematic diagram in Fig. 5(c) to summarize all the key features of the Dirac semimetal of pyrite-type $PtBi_2$ with both the experimental measurements and *ab initio* calculation. It is clear that there are two electron pockets from the linear semimetal band and normal quadratic band, respectively, and a hole pocket from the normal quadratic band. This unique band structure is different from well-studied Cd_3As_2, WTe_2, TaAs, and NbP, and should be related with the observation of extremely large MR in $PtBi_2$.

In conclusion, we have grown high-quality pyrite-type $PtBi_2$ single crystals and performed systemically quantum transport experiments under high magnetic fields. We observed an extremely large MR of $(11.2\times10^6)\%$ at $T = 1.8$ K and $B = 33$T. Such a large MR is even higher than WTe_2, LaSb, and any other Dirac semimetals reported before if the magnetic field is further increased. The crystals exhibit an ultrahigh mobility and clear SdH quantum oscillations. The analysis of quantum oscillations and Hall resistivity have provided detailed electronic structure information about $PtBi_2$, including the multiband characteristics and nontrivial Berry phase that are consistent with our *ab initio* calculation, and provide evidence that $PtBi_2$ is a topological semimetal candidate.

The author thanks Professor Zhiqiang Mao, Dong Qian, and Kun Yang for fruitful discussions. This work was supported by the Natural Science Foundation of China (Grants No. 11574320, No. 11374302, No. 11204312, No. 11474289, No. U1432251, No. 11674311, and No. 11474030), the National Key Research and Development Program of China No. 2016YFA0401003, the 100 Talents Program of Chinese Academy of Sciences (CAS).

W. G., N. H., and F.-W. Z. contributed equally to this work.

*ningwei@hmfl.ac.cn
†xdzhu@hmfl.ac.cn
‡tianml@hmfl.ac.cn

[1] X. G. Wan *et al.*, Phys. Rev. B **83**, 205101 (2011).
[2] M. Orlita *et al.*, Nat. Phys. **10**, 233 (2014).
[3] S. M. Young *et al.*, Phys. Rev. Lett. **108**, 140405 (2012).
[4] Z. J. Wang *et al.*, Phys. Rev. B **85**, 195320 (2012).
[5] Z. J. Wang *et al.*, Phys. Rev. B **88**, 125427 (2013).
[6] C. Fang *et al.*, Phys. Rev. Lett. **108**, 266802 (2012).
[7] Z. K. Liu *et al.* Nat. Mater. **13**, 677 (2014).
[8] M. Neupane *et al.*, Nat. Commun. **5**, 3786 (2014).
[9] S. Borisenko *et al.*, Phys. Rev. Lett. **113**, 027603 (2014).
[10] L. P. He *et al.*, Phys. Rev. Lett. **113**, 246402 (2014).
[11] T. Liang *et al.*, Nat. Mater. **14**, 280 (2015).
[12] Z. K. Liu *et al.*, Science **343**, 864 (2014).
[13] S. Y. Xu *et al.*, Science **347**, 294 (2015).
[14] M. N. Ali *et al.*, Nature (London) **514**, 205 (2014).
[15] S. Y. Xu *et al.*, Science **349**, 613 (2015).
[16] B. Q. Lv *et al.*, Nat. Phys. **11**, 724 (2015).
[17] L. X. Yang *et al.*, Nat. Phys. **11**, 728 (2015).
[18] S. Y. Xu *et al.*, Nat. Phys. **11**, 748 (2015).
[19] S. Y. Xu *et al.* Sci. Adv. **1**, e1501092 (2015).
[20] S. Souma *et al.*, Phys. Rev. B **93**, 161112(R) (2016).
[21] C. Shekhar *et al.*, Nat. Phys. **11**, 645 (2015).
[22] A. Narayanan *et al.*, Phys. Rev. Lett. **114**, 117201 (2015).
[23] Z. Wang *et al.*, Phys. Rev. B **93**, 121112(R) (2016).
[24] Q. D. Gibson *et al.*, Phys. Rev. B **91**, 205128 (2015).
[25] Y. Y. Wang *et al.*, Phys. Rev. B **94**, 041103(R) (2016).
[26] F. F. Tafti *et al.*, Nat. Phys. **12**, 272 (2016).
[27] See Supplemental Material at http://link.aps.org/supplemental/10.1103/PhysRevLett.118.256601 for the detailed analysis of R-T curves under magnetic fields.
[28] Y. L. Wang *et al.*, Phys. Rev. B **92**, 180402(R) (2015).
[29] E. Mun *et al.*, Phys. Rev. B **85**, 035135 (2012).
[30] H. Murakawa *et al.*, Science **342**, 1490 (2013).
[31] G. L. Zheng *et al.*, Phys. Rev. B **93**, 115414 (2016).
[32] D. Shoenberg, *Magnetic Oscillations in Metals* (Cambridge University Press, Cambridge, England, 1984).
[33] C. M. Wang *et al.*, Phys. Rev. Lett. **117**, 077201 (2016).
[34] J. Xiong *et al.*, Phys. Rev. B **86**, 045314 (2012).
[35] Y. K. Luo *et al.*, Phys. Rev. B **92**, 205134 (2015).